CHAPTER IV
EFFECT OF SUPPORT COMPOSITION AND METAL LOADING ON Au CATALYST ACTIVITY IN STEAM REFORMING OF METHANOL*

4.1 Abstract

Gold (Au) supported on CeO_2–Fe_2O_3 catalysts prepared by the deposition-coprecipitation technique were investigated for steam reforming of methanol (SRM). The 3 wt% Au/CeO_2–Fe_2O_3 sample calcined at 400 °C achieved 100 % methanol conversion and 74 % hydrogen yield due to a strong Ce–Fe interaction in the active solid solution phase, $Ce_xFe_{1-x}O_2$. The sintering of Au particles was observed when the highest metal content of 5 wt% was registered, which worsened the SRM activity. According to the TPR and TPO analysis, it was found that the transformation of the α–Fe_2O_3 structure in the mixed oxides and the coke deposition were the main factors for the rapid deactivation of the catalyst.

Keywords: Steam Reforming; Methanol; Hydrogen; Au catalyst; CeO_2; Fe_2O_3

4.2 Introduction

Due to the demand for new energy carriers worldwide, many methods for efficient hydrogen production are still being investigated to find the best candidate [1–3]. Methanol (CH_3OH) is widely acknowledged as a good reactant for the high-purity of hydrogen due to its low boiling point and high H/C ratio, which reduces the soot and coke formation [4–7]. Normally, hydrogen production based on a methanol source can be classified into three main reactions: methanol decomposition (DM), steam reforming (SRM), and partial oxidation (POM). SRM is also an endothermic reaction which obtains the highest H_2 yield (3 moles H_2/1 mole CH_3OH) with lower amounts of CO and low temperature operation (200–400 °C), as shown in Eq (4.1).

$$CH_3OH + H_2O \rightarrow CO_2 + 3H_2 \qquad \Delta H(298\ K) = 50\ kJ\ mol^{-1} \qquad (4.1)$$

---

*International Journal of Hydrogen Energy, 37 (2012) 14072–14084.

However, the activity of SRM reaction depends on the type of catalyst used. Accordingly, it is necessary to produce high H_2 purity which follows the requirement in PEM fuel cells (CO < 10 ppm) [8–10].

Many previous investigations mainly focused on Cu-based catalysts due to their high activity for SRM reaction. Unfortunately, the pyrophoric characteristic seems to be a crucial issue, which causes the rapid deactivation and sintering of these catalysts when the catalyst is carried out at high temperatures (> 270 °C) [11–13]. To avoid this problem, there has been significant activity to develop a new catalyst for this in recent years. Only a few studies related to hydrogen production from methanol over Au-based catalysts are reported; however, this catalyst is well known as an active catalyst in many reactions including preferential CO oxidation (PROX) [14] and water-gas shifted reaction (WGSR) [15]. Yi *et al* found that the Au/CeO_2 catalyst could obtain full methanol conversion at 300 °C over the SRM reaction with no deactivation [11].

The activity of gold catalysts strongly depends on the Au dispersion, Au natural site, Au particle size, and interaction between Au and support (or by itself) [16]. Our previous work found an improvement in Au–Au interaction of 5 wt% Au/CeO_2 catalysts, which facilitated extreme catalytic activity in the oxidative methanol reforming (OSRM) [17]. Ceria (CeO_2) is defined as an interesting support because it has high oxygen storage capacity (OSC) or oxygen vacancy, which allows itself to store and release active oxygen to provide good performance in SRM reaction [18,19]. In further studies, the chemical properties of ceria were successively developed by the incorporation of triple cations, M^{3+} (M = Fe, La, etc), into the ceria lattice [20–22]. This incorporation can enhance the formation of vacancies in the anion sublattice during the charge balancing, where the redox properties in ceria can be improved. The addition of another interesting support, Fe_2O_3, with CeO_2 has been receiving much attention due to the creation of an active solid solution phase ($Ce_xFe_{1-x}O_2$), which could be beneficial for many applications [20,23,24]. The Au/CeO_2–Fe_2O_3 showed high activity for the PROX and WGSR when the strong Ce–Fe interaction was formed in solid solution [25,26]. Based on

previous studies, there are a number of possibilities for catalyst modification by creating oxygen vacancies on the support [27].

In this study, a series of $Au/CeO_2–Fe_2O_3$ catalysts prepared by the deposition-precipitation technique (DP) were investigated for SRM in the temperature range of 200 to 400 °C.

4.3 Experimental

4.3.1 Catalyst preparation

Various ratios of mixed oxides ($CeO_2–Fe_2O_3$) supports—Ce:Fe = 8:1, 1:1, and 1:8—were prepared by a co-precipitation method, while the pure CeO_2 and Fe_2O_3 supports were prepared by a precipitation method. The Au/CeO_2, Au/Fe_2O_3, and $Au/CeO_2–Fe_2O_3$ catalysts were prepared by the deposition-precipitation technique. For support preparation, cerium (III) nitrate hexahydrate ($Ce(NO_3)_3.6H_2O$) (Aldrich), iron (III) nitrate nonahydrate ($Fe(NO_3)_3.9H_2O$) (Aldrich), and Na_2CO_3 (Riedel-de Haen) were mixed under vigorous stirring condition at 80 °C and pH 8. Afterward, the precipitate was washed, dried, and calcined in air at 400 °C for 4 h in order to obtain the $CeO_2–Fe_2O_3$ supports.

Gold was loaded on the supports (CeO_2, Fe_2O_3, and $CeO_2–Fe_2O_3$). An aqueous solution of $HAuCl_4.3H_2O$ (Alfa AESAR) was heated at 80 °C and adjusted to pH 8 with Na_2CO_3. After the resulting solution was stirred for 1 h, the suspension was washed with warm deionized water to eliminate the residue ions. The deionized precipitate was dried at 110 °C and calcined in air at various temperatures (200–400 °C) for 4 h. The $CeO_2–Fe_2O_3$ support at each composition (Ce:Fe atomic ratio) was designated as CeXFeY, where X and Y are the atomic ratio of Ce and Fe, respectively.

4.3.2 Catalyst characterization

The XRD measurement was carried out on a JEOL X-Ray diffractometer system (JDX-3530) with a CuK_α (1.5406 Å) X-ray source operating at 40 kV and 30 mA.

The size and distribution of the Au particles deposited on the supports were directly observed by a transmission electron microscope (JEOL, JEM 2010) at an accelerating voltage of 200 kV in bright field mode. Before being transferred into the TEM chamber, the samples were dispersed in ethanol and were then dropped onto a copper grid. The volume-area average Au particle size diameter (d_{TEM}) was calculated from the following formula: $d_{TEM} = \Sigma(n_i d_i^3)/(n_i d_i^2)$, where n_i is the number of Au particles of diameter d_i.

DR/UV-vis spectroscopy experiments checked for the presence of different states of oxidation of the contained metals (which were recorded on a Shimadzu UV spectrophotometer 2550). The measurements were performed on air-exposed samples between 200 and 800 nm at ambient temperature. The absorption intensity was expressed using the Kubelka-Munk function, $F(R\infty) = (1-R\infty)^2/(2R\infty)$, where $R\infty$ is the diffuse reflectance from a semi-infinite layer. An X-Ray Fluorescence Spectrometry, XRF (AXIOS PW4400) was used to determine the actual surface (Au, Ce, and Fe) composition.

Temperature-programmed reduction (TPR) was utilized for the evaluation of the reducibility of the catalysts and was employed by using 10 % H_2 in Ar at 30 mL/min as a reducing gas in a conventional TPR reactor equipped with a thermal conductivity detector. The reduction temperature was raised from 30 to 850 °C at a ramp rate of 10 °C/min.

The amount of carbon formation of the spent catalysts was measured by means of temperature-programmed oxidation (TPO). Approximately 50 mg of the powdered samples was packed in a quartz tube reactor before being heated from 100 °C with a heating rate of 12 °C/min to 900 °C under a flow of 2 % O_2/He using a gas flow rate of 30 mL/min.

4.3.3 Catalytic activity measurements

The SRM reaction was carried out in a fixed-bed reactor with 80 to 120 mesh holes containing 100 mg of the $Au/CeO_2–Fe_2O_3$ catalysts under atmospheric pressure with a reaction temperature of 200 to 400 °C. A mixture of distilled water and methanol in a syringe was injected continuously by a syringe pump at a rate of 1.5 mL h^{-1} to a vaporizer to produce a vapor of methanol and steam, which was mixed with the He carrier gas before entering the catalytic reactor. The H_2O/CH_3OH molar ratio was fixed constantly at 2/1 since it has been defined as the suitable feed composition for the high catalytic activity of Au catalyst [17]. The Au contents and calcination temperatures were varied from 1 to 5 wt% and 200 to 400 °C, respectively. Finally, the stability of the prepared catalysts was tested for 10 h. The gas hourly space velocity (GHSV) was kept at 21 000 mL/g-cat. h. The product gases (e.g. H_2, CO, CO_2, and CH_4) from the reactor were analyzed both qualitatively and quantitatively by auto-sampling in an on-line gas chromatograph, Agilent 6890N, with a packed carbosphere (80/100 mesh) column (10 ft x 1/8 inch) and a thermal conductivity detector (TCD). The selectivity of each product gas was defined by the mole percentage in the product stream. No methane formation was observed from this study.

4.4 Results and discussion

4.4.1 Catalyst characterization

The chemical and physical properties of the series of $Au/CeO_2–Fe_2O_3$ catalysts are summarized in Table 4.1. The lattice constant of CeO_2 in $CeO_2–Fe_2O_3$ (0.540–0.543 nm) is smaller than that of CeO_2 (0.544), indicating that the presence of Fe_2O_3 resulted in the incorporation of Fe^{3+} (0.064 nm) into the Ce^{4+} (0.101 nm) to form a solid solution [25]. However, with high Fe contents (Ce:Fe = 1:8), these values increased since the segregation of Fe^{3+} from the Ce^{4+} lattice might be more favorable than the $Fe^{3+}–Ce^{4+}$ combination [25], suggesting that high Fe content might prevent solid solution formation.

Table 4.1 Chemical-physical properties of the $Au/CeO_2–Fe_2O_3$ catalysts

Catalyst	Calcination Temperature (°C)	Au (wt%)	Ce (wt%)	Fe (wt%)	Crystallite size[a] (nm)	Lattice constant of CeO_2[b] (nm)	Au crystallite size (nm)		
							d_{111}	d_{200}	d_{220}
3 wt% Au/CeO_2	400	2.74	97.26	-	7.65	0.544	< 5	-	-
3 wt% Au/Ce8Fe1	400	2.27	92.00	5.73	6.78	0.543	7.7	-	-
1 wt% Au/Ce1Fe1	400	1.59	61.02	37.39	6.18	0.540	10.4	-	-
3 wt% Au/Ce1Fe1	400	2.49	61.88	35.63	6.25	0.540	11.9	-	-
3 wt% Au/Ce1Fe1	300	2.60	61.30	36.10	6.82	0.540	11.6	-	-
3 wt% Au/Ce1Fe1	200	2.59	64.46	32.95	6.09	0.540	12.1	-	-
5 wt% Au/Ce1Fe1	400	4.69	58.00	37.31	6.68	0.540	13.9	12.1	6.6
3 wt% Au/Ce1Fe8	400	2.59	76.09	21.32	11.96	0.542	11.3	-	-
3 wt% Au/Fe_2O_3	400	2.57	-	97.43	-	-	10.4	-	-

[a]Mean crystallite sizes were calculated from the average values of CeO_2 plane (111), (220), and (311).

[b]Unit cell parameter calculated from CeO_2 (220) with the Bragg's equation.

The XRD patterns of all studied catalysts are shown in Fig. 4.1A. The strongest diffraction peak of CeO_2 at 2θ = 28.5° represented the fluorite structure [24]. Other positions of weak peaks were also detected, at 33.08, 47.47, 56.33, 59.08, 69.40, 76.69, and 79.07°, corresponding to (200), (220), (311), (222), (400), (331), and (420) for the CuKα (1.5406 Å) radiation, respectively [28,29]. The diffraction patterns of Fe_2O_3, at 24.1, 33.1, 35.6, 40.8, 49.4, 54.0, 57.5, 62.6, and 64.0° (2θ) were due to the presence of hexagonal α-Fe_2O_3 phases that were, respectively, assigned to hematite crystallite planes of (012), (104), (110), (113), (024), (116), (018), (214), and (300) [30,31]. At 3 wt% Au loading, compared to the Au/CeO_2, the intensities of the CeO_2 decreased with increasing Fe content into the mixed oxides (Ce:Fe = 8:1), while the presence of very weak hematite intensities could be associated with the well-dispersed Fe^{3+} incorporating inside the ceria lattice to form CeO_2Fe_{ss} or $Ce_xFe_{1-x}O_2$ solid solution [25,32]. It can be seen that the peaks of the solid solution supports become broader and less intense, suggesting the existence of mixed phases, which dominated the reduction of crystallite sizes [20]. The intensities of hematite peaks became well-defined after increasing the Fe content (Ce:Fe of 1:1), while extreme amounts of Fe added (Ce:Fe = 1:8) provided the sharp peaks of α-Fe_2O_3 . As can be seen from curve e in Fig. 4.1A, the peaks attributed to the spinel structure, appeared in the sample of Ce:Fe = 1:1 and 1:8. This correlated to the crystallinity improvement of the free hematite particles without incorporation of Ce^{4+} inside [25]. Indeed, the insertion of Fe caused a shifting of ceria peaks toward higher diffraction angles, whilst no shifting in hematite phases toward lower diffraction angles was observed in this experiment. Especially for highly concentrated Fe (Ce:Fe = 1:8), in the ranges of 47.5–50° and 56–58°, the intensities of hematite peaks became more pronounced and started to shift away from the overlapped regions of mixed phases, evidenced by the segregation of Fe^{3+} from the ceria lattice to form the pure hematite phase. Consequently, the lattice constant was increased with the excess Fe, which exhibited more segregated or free α-Fe_2O_3.

Interestingly, the significant difference in peak intensities of Au (111) at 38.5° became detectable at high Fe contents probably due to the variation in gold dispersion affected by Fe concentration. Based on the Scherrer equation, the

crystallite sizes of the Au (111) were detectable in the high Ce concentration (Ce:Fe = 8:1).Moreover, high Fe amounts could enlarge the Au crystallite sizes (10–11 nm), leading to speculation that the strong intermetallic bonding of Au–Fe could form the Au cluster (Au_n, $1 < n < 10$) which enhanced the Au crystallinity [33,34]. When the amount of Au loading reached 5 wt%, a significant increase in crystallinity of the Au (111) was clearly observed in Fig. 4.1B, including the appearance of Au (200) and Au (220) reflections at $2\theta = 44.4°$ and 64.6° [35], respectively. This result suggested that an agglomeration of the gold particles occurred, and then resulted in larger Au particle size. The Au crystallite size increased from 10.4 nm to 13.9 nm with an increasing of Au loading from 1 to 5 wt%, indicating the growth of Au nanoparticles [36].

In Fig. 4.1C, the high crystallinity of both Au (111) and CeO_2 peaks were observed when the calcination temperature was lower than 400 °C. In addition, the appearances of high α–Fe_2O_3 intensities were also observed at these low temperatures. A possible explanation could be the generation of free α–Fe_2O_3 particles separating from the solid solution phase and then becoming soluble with Au to facilitate more Au clusters or Au crystallinity, as reported previously. As a result, the calcination temperature of 400 °C seemed to broaden the ceria diffraction peaks, including lowering crystallinity, representing the best incorporation of Fe^{3+} in Ce^{4+} for homogeneous solid solution creation. The similar explanation of broaden peaks was also reported in mixed oxides, such as CeO_2–ZrO_2 [37]. In addition, the broadening of the ceria is attributed to either a decrease of ceria crystallite size or oxygen vacancies.

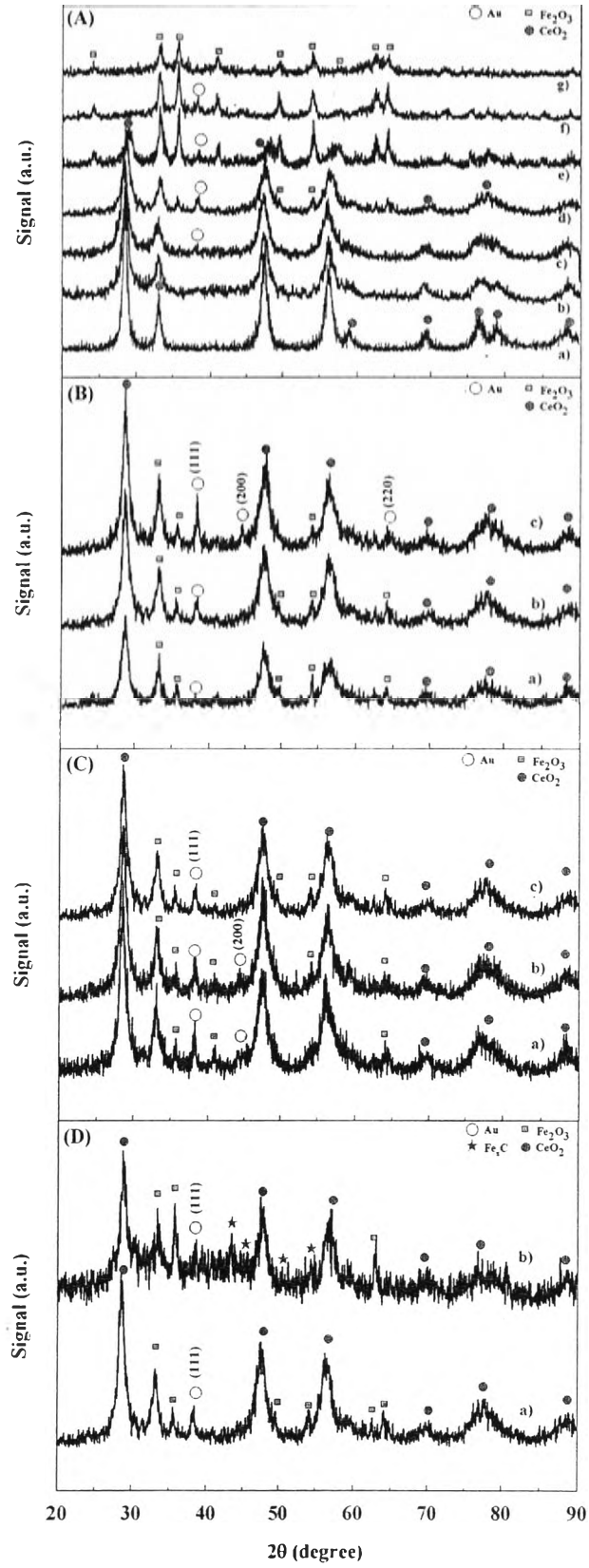
(A)
Au
Fe_2O_3
CeO_2
g)
f)
e)
d)
c)
b)
a)
Signal (a.u.)
(B)
Au
Fe_2O_3
CeO_2
(111)
(200)
(220)
c)
b)
a)
Signal (a.u.)
(C)
Au
Fe_2O_3
CeO_2
(111)
(200)
c)
b)
a)
Signal (a.u.)
(D)
Au
Fe_3C
Fe_2O_3
CeO_2
(111)
b)
(111)
a)
Signal (a.u.)
20
30
40
50
60
70
80
90
2θ (degree)

Figure 4.1 XRD patterns of the Au/CeO_2–Fe_2O_3 catalysts: (A) Effect of support compositions calcined at 400 °C; (a) CeO_2, (b) 3 wt% Au/CeO_2, (c) 3 wt% Au/Ce8Fe1, (d) 3 wt% Au/Ce1Fe1, (e) 3 wt% Au/Ce1Fe8, (f) 3 wt% Au/Fe_2O_3, and (g) Fe_2O_3. (B) Effect of Au loadings; (a) 1 wt% Au/Ce1Fe1, (b) 3 wt% Au/Ce1Fe1, and (c) 5 wt% Au/Ce1Fe1. (C) Effect of calcination temperatures on 3 wt% Au/Ce1Fe1; (a) calcined at 200 °C, (b) calcined at 300 °C, and (c) calcined at 400 °C. (D) Comparison between (a) fresh catalyst and (b) spent catalyst.

4.4.2 Catalytic activity

4.4.2.1 Effect of support composition

Fig. 4.2 (A, B) presents the catalytic activities of supports and supported Au catalysts. In the absence of Au deposition, the pure CeO_2 and Fe_2O_3 supports showed low catalytic activities in the reaction temperatures studied, whilst CeO_2–Fe_2O_3 (Ce:Fe = 1:1) significantly enhanced either methanol conversion or product gases concentrations. Focusing on the supported Au catalysts with 3wt% Au, an increase of methanol conversion as the functional reaction temperature was observed in all samples. Interestingly, Au catalysts demonstrated much better catalytic performance than those of the supports without Au loading, indicating that the presence of the active Au metal was necessary to efficiently promote catalytic activity. In terms of product composition in the Au catalysts, it was found that the H_2 and CO concentration (%) increased with reaction temperature, where the methanol decomposition could appear at high temperatures during the SRM reaction. The mole percentage of CO was still quite low in the range of 0–3.2 %, while the H_2 concentration seemed to have the same trends as the methanol conversion, and its maximum value of 38 % was observed at the highest temperature.

In terms of gas selectivity (Fig. 4.2 bar graph), the roles of Au loading was clearly observed in decreasing CO selectivity and increasing H_2 selectivity in the entire range of reaction temperatures. Indeed, when compared to another catalyst, CuO–CeO_2 [1], our catalysts were considered as more active catalysts with less CO formation. This could be implied that the Au catalyst plays an important role in CO reduction in SRM. The support composition (Ce:Fe) directly

influenced the SRM activity as ordered: 1:1 > 8:1 > 1:0 > 1:8 > 0:1. High catalytic activity was observed when the amounts of Fe_2O_3 were initially registered, denoted as Ce:Fe (1:1) and (8:1). For the catalysts with a high amount of Fe_2O_3 (Ce:Fe = 1:8 and pure Fe_2O_3), the catalytic behavior was suppressed when the Fe concentration was higher than the optimum value, Au/Fe_2O_3 displayed the lowest activity. The results obtained from the prepared catalysts agree perfectly with the trends reported by Yonggang *et al.*, who concluded that its high activity could be attributed to the solid solution formation and good dispersion of Fe_2O_3 on the catalyst surface [38]. As mentioned above, the $Au/CeO_2–Fe_2O_3$ (1:1) was the best catalyst, which obtained 100 % methanol conversion, 74 % hydrogen yield, and 38 % mole H_2 at 400 °C. In this experiment, the hydrogen yield was not shown since it followed the same trend as the methanol conversion.

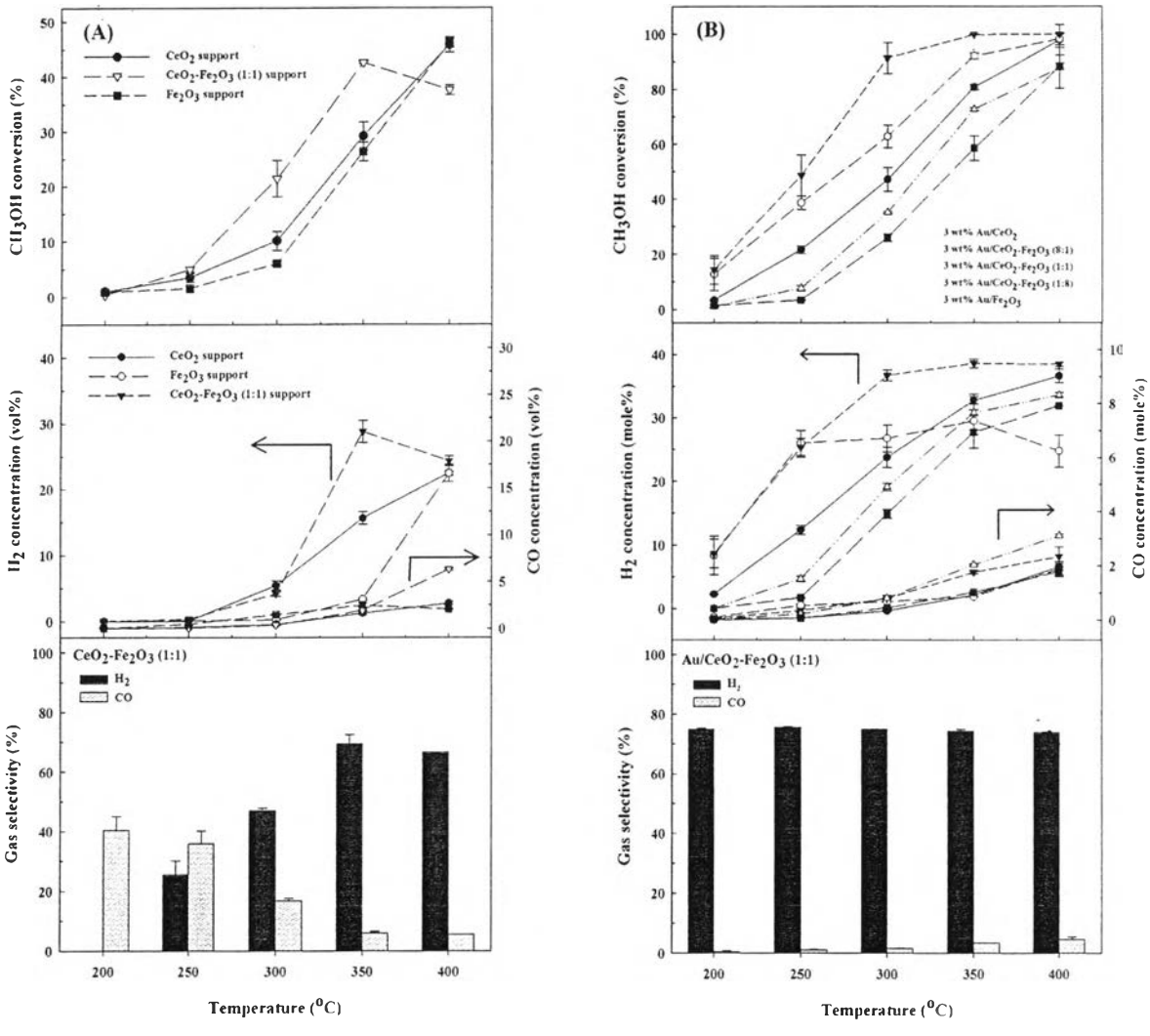

Figure 4.2 Effect of support composition on methanol conversion and product compositions over: (A) support without Au deposition; and (B) Au/CeO_2–Fe_2O_3. (Reaction conditions: H_2O/CH_3OH, 2/1; calcination temperature, 400 °C.)

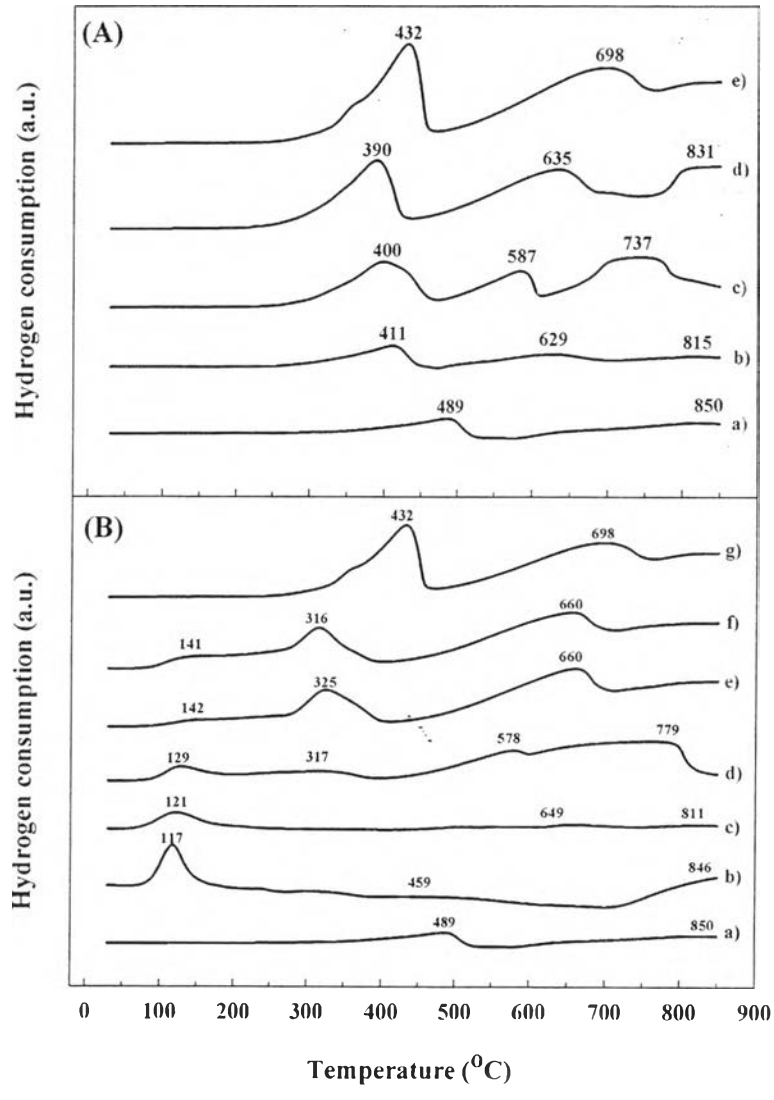

Figure 4.3 TPR profiles of the samples: (A) without Au deposition; (a) CeO_2, (b) Ce8Fe1, (c) Ce1Fe1, (d) Ce1Fe8, and (e) Fe_2O_3. (B) with Au deposition; (a) CeO_2, (b) 3 wt% Au/CeO_2, (c) 3 wt% Au/Ce8Fe1, (d) 3 wt% Au/Ce1Fe1, (e) 3 wt% Au/Ce1Fe8, (f) 3 wt% Au/Fe_2O_3, and (g) Fe_2O_3.

According to the TPR profiles of the supports (Fig. 4.3A), the ceria presented a broader peak situated close to 489 °C, which is typically related to an oxygen surface reduction process, and the other at a higher temperature (around 850 °C), which is linked to the bulk reduction from the ceria structure (CeO_2 to Ce_3O_4) [39–41]. In the two-step reduction of Fe_2O_3, the first peak at 432 °C was

associated with the hematite-to-magnetite transformation ($Fe_2O_3 \rightarrow Fe_3O_4$), which then transformed to metallic iron ($Fe_3O_4 \rightarrow FeO \rightarrow Fe$) at 698 °C [42–44]. In comparison to the pure CeO_2 and Fe_2O_3, the mixed oxides showed three reduction peaks; the first peak was related to the hematite-to-magnetite state or the reduction of Fe^{3+} located on the surface [45]; the second peak was possibly associated with the overlapping of the reduction of Ce^{4+} and the reduction of Fe^{2+}; and the last peak was attributed to the reduction of bulk CeO_2 [46].

It is well known that the generation of oxygen vacancies could result in active oxygen releasing. The presence of Fe could enhance reducibility of the catalysts by shifting reduction peaks toward a lower temperature, when compared to the pure CeO_2. This shifting behavior was evidenced by the strong Ce–Fe interaction where the hematite-like solid solution could be formed [25,47]. Besides, the intensity of the peak at 400 °C gradually strengthened with increasing Fe content, implying that the more free α-Fe_2O_3 generated in the rich-Fe samples, the more Fe^{3+} reductive species were created, as evidenced in the increased intensity of Fe_2O_3 diffractions in the XRD [45]. According to the TPR and XRD results, the coexistence of solid solution and free α-Fe_2O_3 particles in Ce:Fe of 1:1 could indicate the interaction between the free α-Fe_2O_3 particles and solid solution, which exhibited the best redox properties. Some authors also found a similar interaction between NiO particles and Ce–Ni solid solution, playing a significant role in the reducibility improvement of the catalyst [48]. In contrast, the Ce:Fe of the 1:8 sample had no solid solution (according to the high lattice constant), but it was reduced faster than the pure CeO_2, and the intensity of the Fe^{3+} peak at 390 °C became pronounced. This infers that the interaction between free α-Fe_2O_3 particles or free Fe^{3+} species and CeO_2 is still possible for the reduction behavior in the Ce–Fe system [45].

From the TPR profiles of Au/CeO_2–Fe_2O_3 catalysts (Fig. 4.3B), the T_{max} at very low temperatures (117–142 °C) illustrated the reduction of the Au_xO_y species (or Au hydroxide) to Au metal (Au^0) [49,50]. The deposition of Au particles could improve the reducibility of all supports where the shifting reduction peaks toward lower temperatures correlated to the strong metal–support interactions (Au–Fe and Au–Ce) [30,44,51]. The improvement in reducibility of Au/Fe_2O_3

catalysts has been proposed by the kinetic mechanisms [42,52];furthermore, some authors signified that the weakening of the Fe–O bond by another metal as the main reason for simple reduction [53]. The simplest reducibility of Au nanoparticles belonged to the Au/CeO_2 catalyst with the highest quantity of H_2 consumption (or area under its reduction peak), when compared with Au/CeO_2–Fe_2O_3. According to small amount of hydrogen consumed, it has been suggested that Au could form very strong intermetallic bonds with Fe due to the slight solubility of Fe in gold [33,34];therefore, the gold clusters (Au_n) with less reducibility than $Au^{\delta+}$ might be favored [33] and possibly increase the Au crystallite size. This was in line with the appearance of Au (111) at high Fe concentrations in the XRD patterns. Apparently, the trends of Ce–Fe interaction were similar to those without Au deposited, implying the similarity of solid solution form. The optimal ratio of Ce:Fe at 1:1 still gave the three closest reduction peaks; hematite-to-magnetite reduction (317 °C); the likely-combination between Fe^{2+} and Ce^{4+} reduction (578 °C); and magnetite-to-metallic iron (779 °C) where the strongest Ce–Fe interaction in $Ce_{1-x}Fe_xO_2$ solid solution occurred [25].

When focusing on the Au–support interaction, the Au_xO_y peak shifted toward higher temperatures with increasing Fe content, and stayed closer to the Fe^{3+} reduction (316–325 °C), as shown in the Ce:Fe sample of 1:1, 1:8, and pure Fe_2O_3. This suggested an improvement in the interaction between the Au_xO_y and CeO_2–Fe_2O_3 support. However, the Au/CeO_2–Fe_2O_3 (1:1) catalyst obviously indicated a stronger interaction between the Au_xO_y and the Fe^{3+} in the solid solution phase, which strongly facilitated the catalytic activity. Although the strength of the Au–Fe^{3+} interaction in Ce:Fe of 1:8 and pure Fe_2O_3 were still high, the Fe^{3+} interaction mainly came from the free α-Fe_2O_3, as evidenced in the increasing intensity of the Fe^{3+} reduction, which was less active than the solid solution. Consequently, the strongest Au–free Fe^{3+} interaction in Ce:Fe of 1:8 and pure Fe_2O_3 did not always enhance SRM activity since Au sintering and the lack of solid solution phase dominated the activity instead. The evolution of free Fe_2O_3 particles, via XRD, has been identified as Fe segregation from the solid solution, which reduced the active catalysts by weakening the Ce–O–Fe interaction [54]. We

postulated that the strong Au–Fe^{3+} interaction in the solid solution, not free Fe^{3+}, seemed to increase the reaction in this case.

To provide a uniform solid solution, the limitation of Fe^{3+} doping must be considered [55,56]. It was strongly noted that the solubility limit of iron in the ceria lattice depends on many conditions, such as the preparation technique [54], calcination temperature [45], and precursor [54]. However, our optimal catalyst conditions, with a Ce:Fe ratio of 1:1 calcined at 400 °C, prepared by the coprecipitation technique demonstrated the solubility limit of iron in the ceria matrix, while the excess Fe caused Fe^{3+} segregation from the ceria lattice.

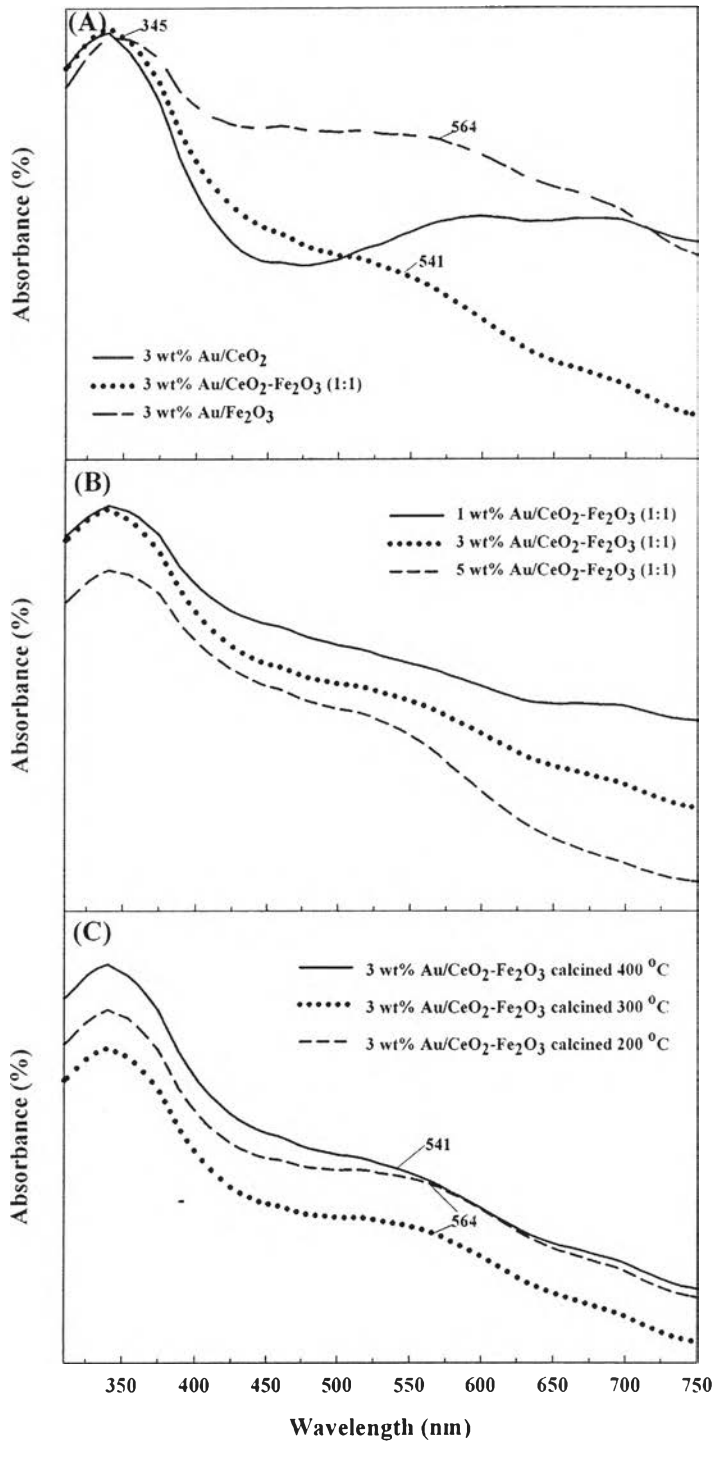

Figure 4.4 Diffuse reflectance UV–vis spectra of the Au species: (A) Effect of support compositions, (B) Effect of Au loadings, and (C) Effect of calcination temperature.

UV-vis spectra measurements were used to identify the Au species, which were responsible for the catalytic activity, as shown in Fig. 4.4A. The plasma band that centered at around 340 nm could be related to the CeO_2, and the Fe_2O_3 that typically shows two plasma bands at 345 nm and 564 nm [31]. For the mixed oxide, the broaden CeO_2 peak and the shifting in Fe_2O_3 peak with low intensity at 541 nm indicated the incorporation of Fe^{3+} in the Ce^{4+} for solid solution creation. A similar observation of this mixed phase has been recorded with the same technique [23]. Normally, the plasma band in the range of 500–600 nm and < 250 nm are defined as the gold plasmon or Au metallic (Au^0) species [57] and Au^{3+} species, respectively [58], and Au clusters (Au_n) can be observed at 280–380 nm [59]. Only the Au^0 species in the Au/CeO_2 catalyst was detectable, whereas those of Au/Fe_2O_3 and $Au/CeO_2–Fe_2O_3$ catalysts were impossible to detect due to the interference of supports and the resonance band of various gold species.

4.4.2.2 Effect of Au content

It is well known that the amount of Au content causes a strong effect on catalytic activity. In this experiment, catalytic activity increased significantly with increasing amounts of Au from 1 wt% to 3 wt%, while the highest Au content (5 wt%) conversely exhibited lower activity, as illustrated in Fig. 4.5. The mole percentage of CO was still observed in the minute values of 0–3.2 %, while the gap difference of %mole H_2 became larger, the same as in the methanol conversion, after increasing the Au loading to 3% and 5%, respectively. These results revealed that the active Au metal is very effective in SRM activity. The 3 wt% Au sample was determined to be the most suitable content for SRM reaction, which promoted high dispersion, including optimum gold particle size. It is not in good agreement with recent findings with 1 wt% Au in our previous work, which exhibited the highest activity for PROX [60].

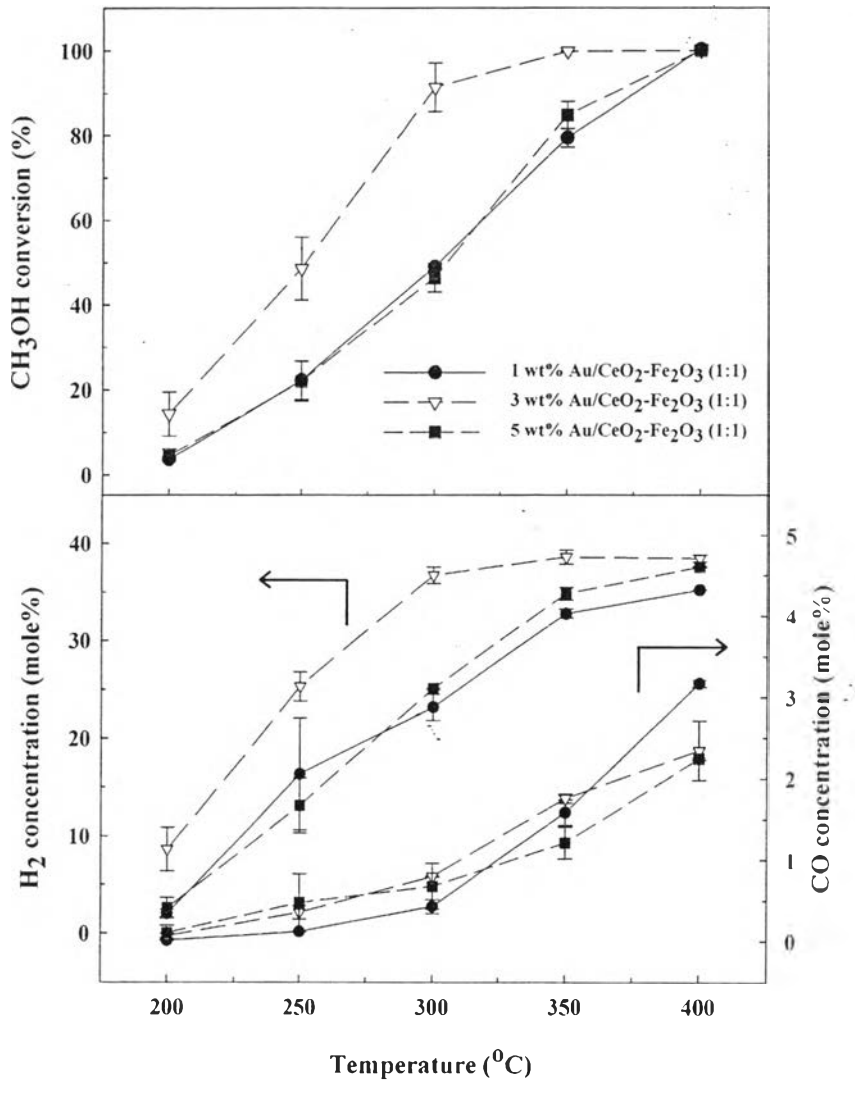

Figure 4.5 Effect of Au loading on methanol conversion and product compositions over $Au/CeO_2–Fe_2O_3$. (Reaction conditions: H_2O/CH_3OH, 2/1; calcination temperature, 400 °C.)

As illustrated in Fig. 4.6A, TPR profiles of Au catalyst with different Au loadings revealed that the hematite reduction shifted toward lower a temperature (275 °C), while two remaining reduction peaks shifted toward higher temperatures (591 and 805 °C) after depositing the lowest Au content. This could be referred to either weaker support–support (Ce–Fe) interaction in free $\alpha–Fe_2O_3$ or less dispersed Fe in the mixed oxides, resulting in insufficient sites of solid solution. A similar kind of free metal oxide with less interaction on the catalyst surface was also

reported [37]. Only a slight change in Au reduction temperature was observed when the Au loading was higher than 1%. With the decrease in the amount of H_2 which was consumed in Au reduction peak, the quantities of various Au species could be correlated with increasing Au loading. The amount of Au^0 species was high in the presence of 3 wt% and 5 wt% Au, while 1 wt% Au contained many $Au^{\delta+}$ species. Our speculation is that 3 wt% Au created suitable Au^0 and $Au^{\delta+}$ content to form the optimum Au particle size. When the amount of 5 wt% Au was deposited, the diminution of H_2 consumed indicated the depletion of the concentration of Au/CeO_2–Fe_2O_3 interphase sites because an agglomeration of Au nanoparticles (promoting ultra Au^0 content) possibly inhibited the catalytic activity of Au catalyst [41]. This explanation also followed the trends of XRD patterns. Nevertheless, the variety of $Au^{\delta+}$, Au^0, and Au_n appearances is regarded as the key parameter for PROX, while WGS reaction has not been yet clarified [16]. Some authors mention that the co-existence of Au_n and Au^0 has no more active than only the Au^0 specie [61]. It has been suggested that the activity of the catalysts strongly depend on the Au^0 presented on the surface and the strength of each interaction type as well.

Based on the UV-spectra shown in Fig. 4.4B, this technique can be used to analyze qualitatively the Au sintering by considering the increase in intensity (or area) of the Au^0 plasma band in 5 wt% Au. Additionally, the TEM images were also used to estimate the Au particle size—the dark spots on the supports—and their distributions, as imaged in Fig. 4.7 (a–c). The mean Au particle sizes at 1, 3, and 5 wt% Au loadings were 23.53, 43.07, and 62.57 nm, respectively. The results agreed with many previous characterizations, where 5 wt% Au presented the largest Au particle sizes, attributing to complete sintering. It should be noted that the suitable Au particle size for the SRM activity was approximately 43 nm.

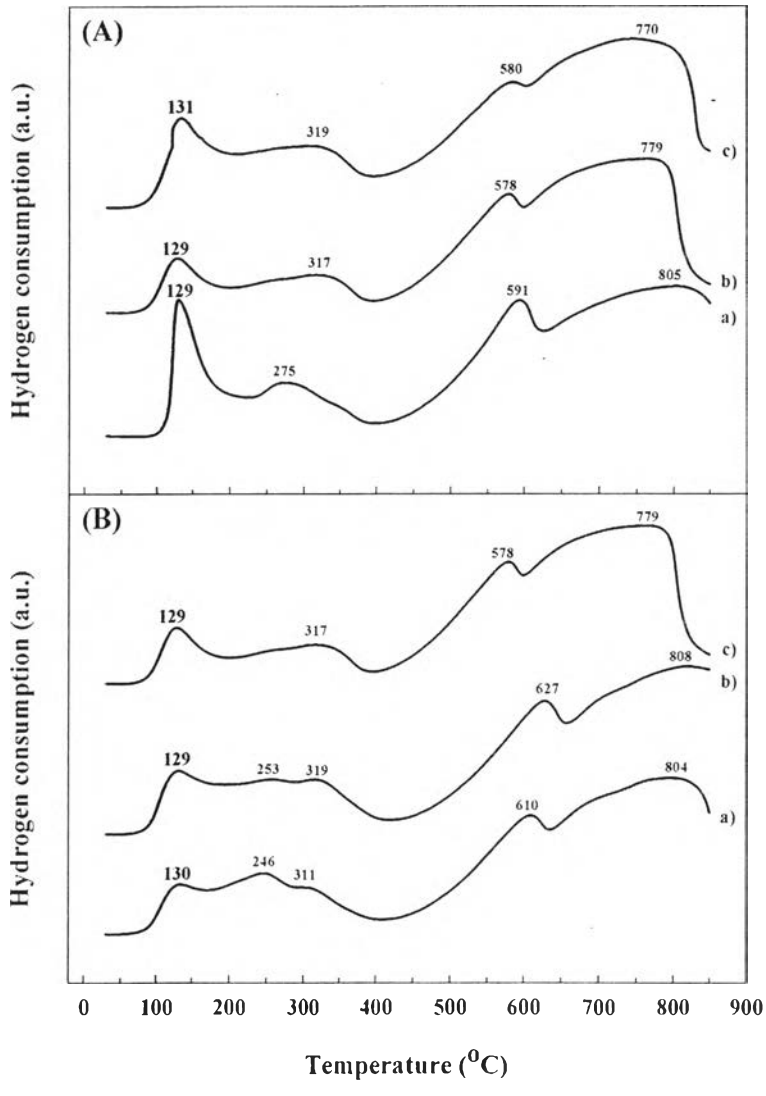

Figure 4.6 TPR profiles of the Au/CeO_2–Fe_2O_3 catalysts: (A) calcined at 400 °C with various Au loadings; (a) 1 wt% Au/Ce1Fe1, (b) 3 wt% Au/Ce1Fe1, and (c) 5 wt% Au/Ce1Fe1. (B) with different calcination temperatures; (a) calcined at 200 °C, (b) calcined at 300 °C, and (c) calcined at 400 °C.

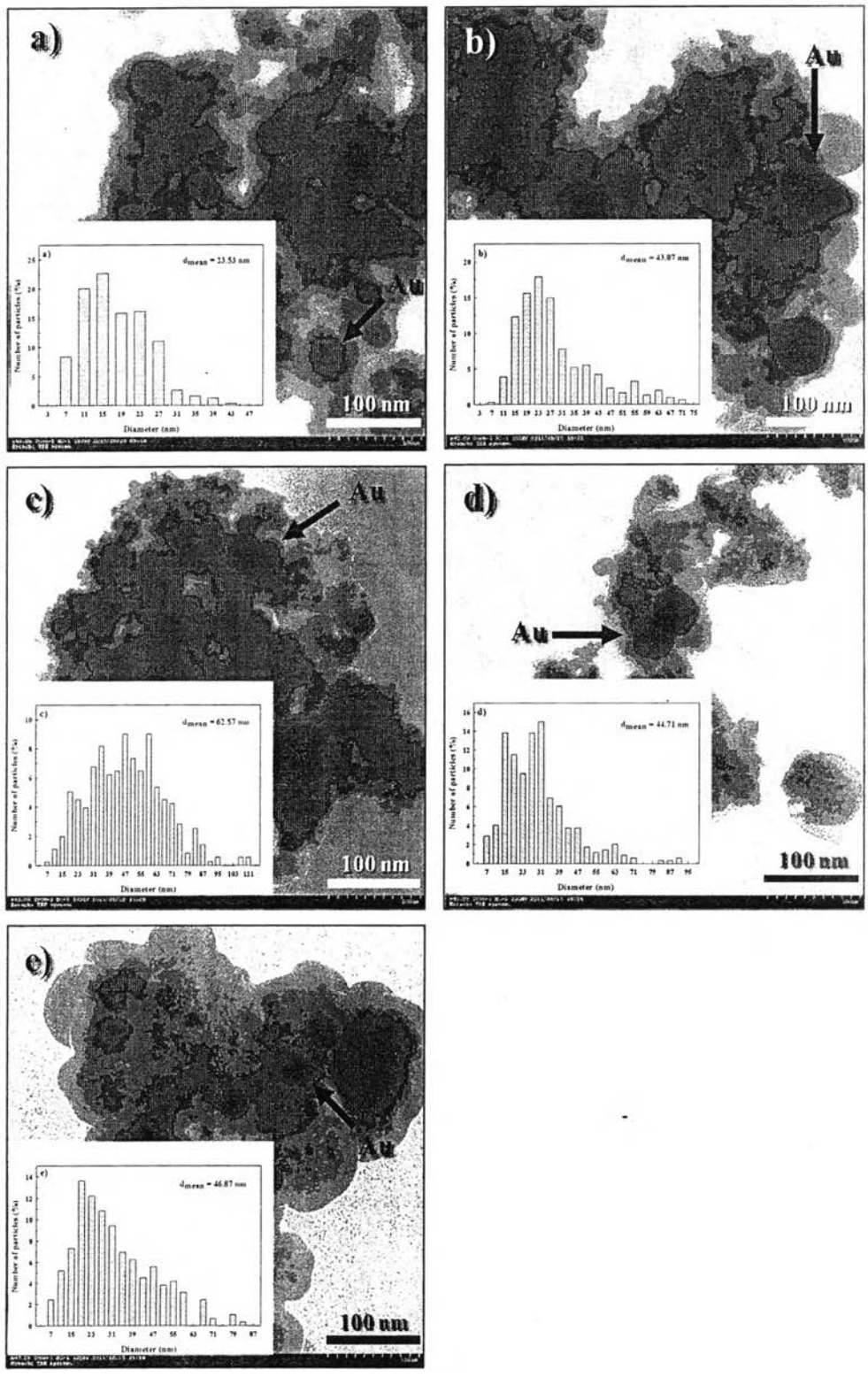

Figure 4.7 TEM images and Au particle size distributions (insets): (a) 1 wt% Au/CeIFeI; (b) 3 wt% Au/CeIFeI; (c) 5 wt% Au/CeIFeI; (d) 3 wt% Au/CeIFeI calcined at 200 °C; and (e) 3 wt% Au/CeIFeI calcined at 300 °C.

4.4.2.3 Effect of calcination temperature

As reported in Fig. 4.8, the high activity with %mole H_2 of 3 wt% Au/CeO_2–Fe_2O_3 (1:1) was not observed when the calcination temperature was lower than 400 °C. In addition, the lowest percentage of mole CO was found in the catalyst calcined at 400 °C, while the higher CO concentrations were observed at lower the calcination temperatures. However, the highest %mole CO was still less than 5 %. It could also be implied that the performance during the production of H_2 gas and the reduction of CO during the SRM reaction was possibly affected by the thermal treatment. The suitable condition for thermal treatment should be 400 °C since this temperature provided sufficient interaction and crystallization for solid solution. We postulated that higher calcination temperatures were significant for the catalyst solid solution properties in the SRM reaction.

The TPR profiles, presented in Fig. 4.6B, show two more separation peaks of free α–Fe_2O_3 reduction, corresponding to two types of free α–Fe_2O_3 particle, at low calcination temperature. The first type could be classified as larger free Fe_2O_3 particles that have less support–support interaction (or strong Fe–Fe interaction), which then require the lower reduction temperatures (253 and 246 °C). Another type at a higher reduction of temperature (319 and 311 °C) has small Fe_2O_3 particles associated with a stronger interaction. Conversely, the strong metal–support interaction between Au and the large free Fe_2O_3 particles corresponded to the overlapping of the reduction peaks at a low calcination temperature. Accordingly, more Au_n might be generated as well. Interestingly, the 200 °C treatment gave the sharpest peak of the large free α–Fe_2O_3 particles compared with the broader peak at the calcination temperature of 300 °C. This might be due to the lack of homogeneous dispersion of the hematite phase in the mixed oxide support, which can be estimated from the width of the hematite peak [37], so the chance of free α–Fe_2O_3 generation would be higher with decreasing calcination temperature. It should be noted that the broader the reduction peak the free α–Fe_2O_3 has, the better the dispersion and interaction of homogeneous free α–Fe_2O_3 becomes. In conclusion, the increase in calcination temperature led to the fully developed solid solution phase homogeneity

where two types/peaks of free α–Fe_2O_3 turned to combine completely in this experiment.

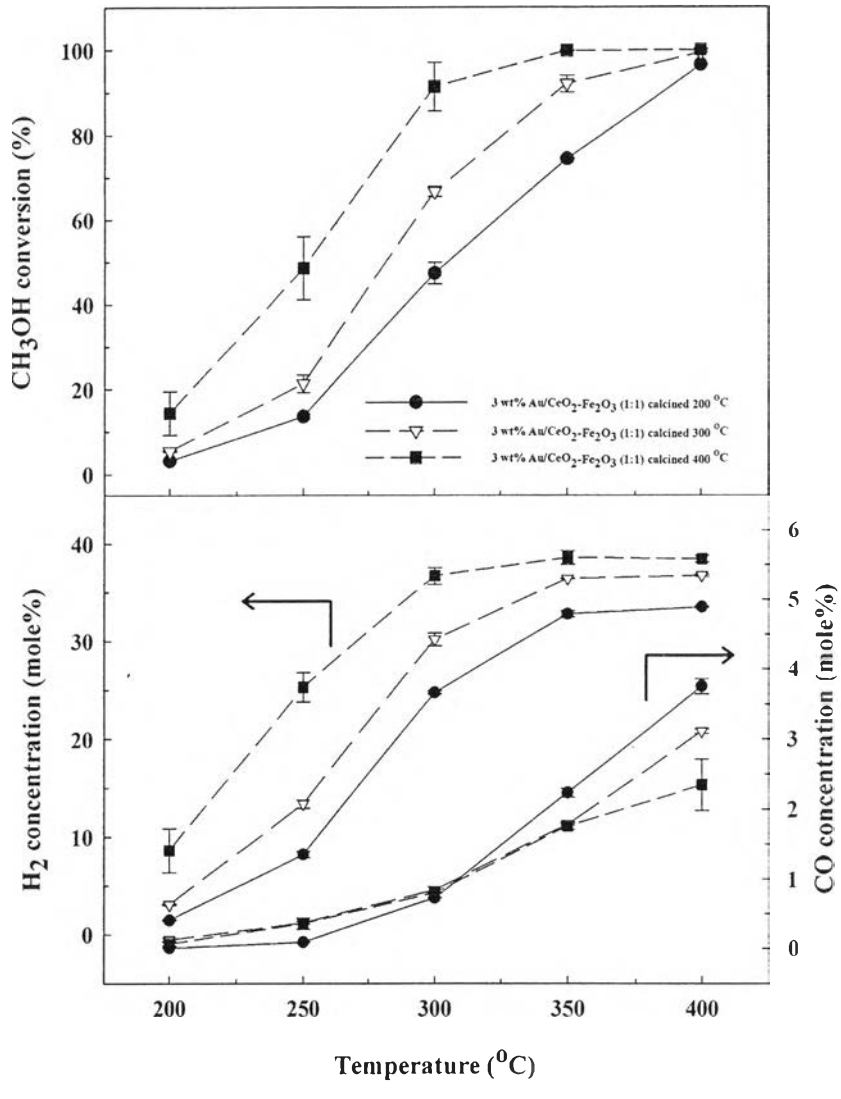

Figure 4.8 Effect of calcination temperature on methanol conversion and product compositions over 3 wt% Au/Ce1Fe1. (Reaction condition: H_2O/CH_3OH, 2/1)

As mentioned above, the XRD patterns (Fig. 4.1C) signified the dispersion of homogeneous α–Fe_2O_3 on the ceria lattice where the intensities of ceria peaks were broadened with increasing calcination temperature. In particular, one diffraction angle of α–Fe_2O_3 at 40.8° appeared at the lowest calcination temperature because the fact that the large free α–Fe_2O_3 particle was favored and easily detected on the surface of the catalyst. This kind of observation has been

reported in free NiO catalysts [37]. On the other hand, the intensity and crystallite size of Au (111) was the most pronounced at the lowest temperature, corresponding to the larger Au particle sizes which might come from the combination between Au_n and Au^0 species.

Focusing on the UV-spectra in the Fig. 4.4C, the shifting in spectrum peaks (from 541 to 564 nm) were observed for low calcination temperatures. This represented the creation of free α–Fe_2O_3 without homogeneous solid solution form, $Ce_{1-x}Fe_xO_2$. From TEM results in Fig. 4.7(b, d, and e), the mean particle sizes of the Au, with calcination temperatures of 200, 300, and 400 °C, were, respectively, 46.87, 44.71, and 43.07 nm. Although Au catalysts calcined at 300 and 400 °C were a similar particle sizes. The largest Au particle calcined at 200 °C showed slight agglomeration, which was in line with the Au_n formation originating from the strong interaction of Au–Fe (large free α–Fe_2O_3 particle). We, therefore, elucidated the homogeneity of solid solution phase and the Au sintering as the main factors for lowering the catalytic activity.

4.4.3 Stability testing

As illustrated in Fig. 4.9, the stability of 3 wt% Au/CeO_2–Fe_2O_3 calcined at 400 °C without O_2 pretreatment was tested for SRM at a H_2O/CH_3OH molar ratio of 2/1 at 400 °C for 10 h. The methanol conversion and hydrogen yield were found to drop rapidly from 100 % and 74 % (at the initial time) to the average values of 25.9 % and 19.3 %, respectively, after 96 minutes. The selectivity of H_2, CO, and CO_2 gases were 75.5, 20.5, and 5 %, respectively. The decline in conversion could be attributed to the coke formation [29] via the carbon monoxide disproportionation reaction or the rapid consumption of surface-adsorbed oxygen during the experiment. In addition, it is well known that gold-based catalysts are more susceptible to thermal sintering than other commonly used catalysts, resulting in the sintering of the gold crystallites, and consequent loss of catalytic activity.

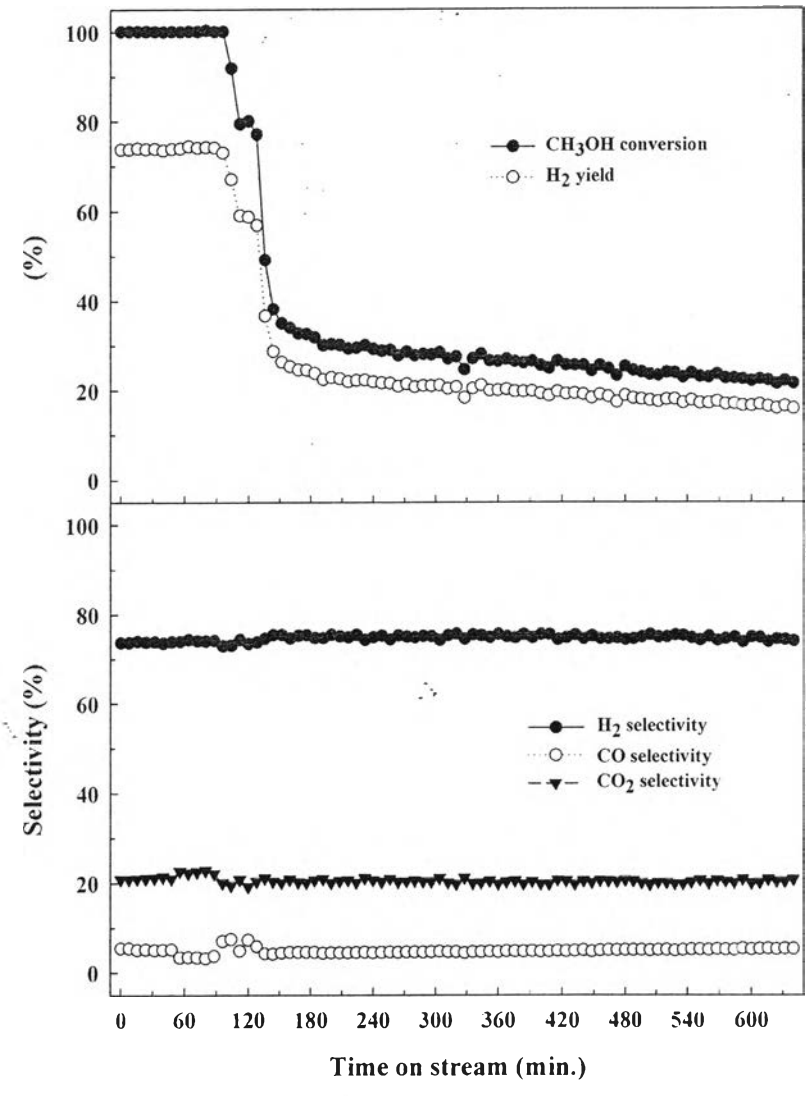

Figure 4.9 Stability observation of 3 wt% Au/Ce1Fe1 catalyst calcined at 400 °C. (Reaction conditions: H_2O/CH_3OH, 2/1; reaction temperature, 400 °C; and time-on-stream per sample, 10 h)

To analyze the amount of coke deposited on the catalyst surface, the TPO profiles of spent catalysts, as illustrated in Fig. 4.10, show two distinct peaks of coke formed: i) low-temperature oxidation at 285, 312, and 320 °C assigned to the oxidation of the poorly polymerized coke deposited on the metal particles and ii) high-temperature oxidation at 492, 512, and 593 °C attributed to highly polymerized coke deposited near the metal–support interphase [62]. The types of coke formed on

the catalyst surface have been classified based on the reaction temperature and the type of reaction [63–65]. In this work, the results revealed that the amount of coke deposited on the metal was higher than that on the support, and the coke percentage in the spent catalyst was 2.60 wt%. However, the fresh catalyst showed the lowest temperature at 106 °C, which was related to the oxidation of carbonate species, not the coke [11].

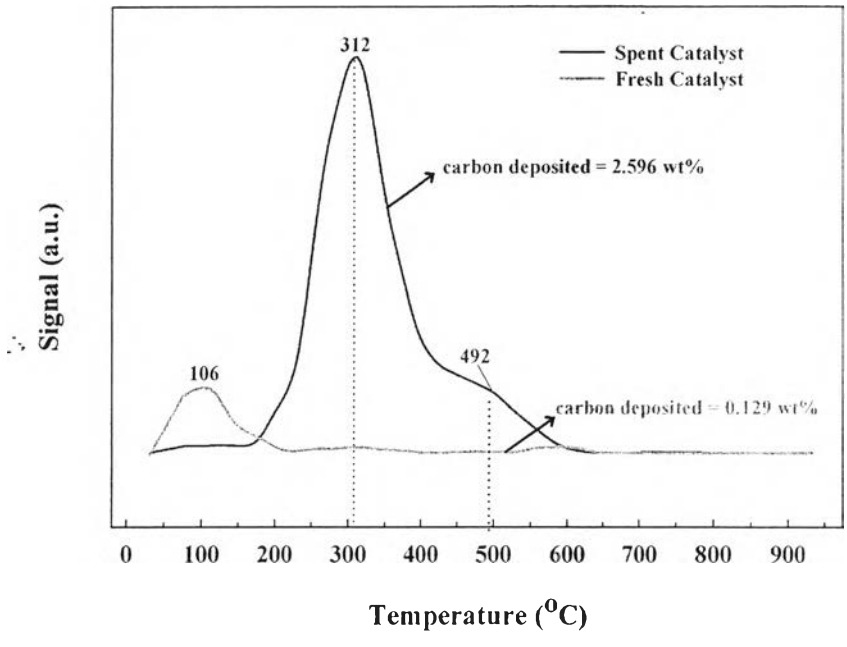

Figure 4.10 TPO profiles of spent 3 wt% Au/CeIFeI catalyst after exposure to reaction compared with the fresh catalyst. (Reaction conditions: H_2O/CH_3OH, 2/1; reaction temperature, 400 °C; and time-on-stream per sample, 10 h)

The XRD patterns of the spent catalysts are presented in Fig. 4.1D. The unchanged CeO_2 diffraction peaks were detected and some diffraction peaks of α–Fe_2O_3 disappeared, implying that the coke partially covered the α–Fe_2O_3 surface. In addition, some angles of α–Fe_2O_3 (35.6° and 62.6°) seemed to lead to improved crystallinity, which possibly came from the sintering of Fe_2O_3 particles during the stability test. On the other hand, this might represent the segregation of the free Fe_2O_3 particles from the solid solution phase, indicating the lack of solid solution during the SRM reaction. Particularly, the peak of carbon iron chemical compounds

(Fe_xC) was also visible. This appearance could confirm that coke remained on the spent catalyst surface. To support the above explanation, Knogzhai *et al.* also defined the Fe_3C as massive carbon depositions on the spent catalyst, detected by an XRD machine [20]. Accordingly, the formation of Fe_xC in our work might be the consequence of the reduction of Fe_2O_3 via the deposited carbon, or via the H_2 product gas, followed by the carbon interaction during the reaction. In conclusion, we speculated that the factors for the $Au/CeO_2–Fe_2O_3$ deactivation were mainly from the lack of the homogeneous solid solution phase and coke deposition.

4.5 Conclusions

The $Au/CeO_2–Fe_2O_3$ catalysts have been developed for SRM to produce high purity H_2 in the temperature range of 200 to 400 °C. Initial catalytic activity was successfully achieved by mixing Fe_2O_3 and CeO_2 equally with the Ce:Fe atomic ratio of 1:1 to form the active solid solution phase. Moderate amounts of Au deposited (3 wt%) on the mixed oxides support calcined at 400 °C seemed to be the optimum condition without providing Au sintering. Nevertheless, the sintering of hematite particles was further considered as one of the parameters for the loss in activity of the $Au/CeO_2–Fe_2O_3$ catalyst, while Au sintering was not involved in this case. Our findings suggest that the reducibility of the support may affect the catalyst properties and the catalytic activities for SRM.

4.6 Acknowledgements

The authors acknowledge the contributions and financial support of the following organizations: the Thailand Research Fund through the Royal Golden Jubilee Ph.D. Program (Grant No. PHD/0282/2552); the National Center of Excellence for Petroleum, Petrochemicals, and Advanced Materials, Chulalongkorn University; and The National Research University Project of CHE and the Ratchadaphiseksomphot Endowment Fund (EN276B).

4.7 References

[1] Udani PPC, Gunawardana PVDS, Lee HC, Kim DH. Steam reforming and oxidative steam reforming of methanol over CuO–CeO_2 catalysts. Int. J. Hydrogen Energy 2009; 34: 7648–55.

[2] Patel S, Pant KK. Kinetic modeling of oxidative steam reforming of methanol over Cu/ZnO/CeO_2/Al_2O_3 catalyst. Appl. Catal., A 2009; 356: 189–200.

[3] Manzoli M, Chiorino A, Boccuzzi F. Decomposition and combined reforming of methanol to hydrogen: a FTIR and QMS study on Cu and Au catalysts supported on ZnO and TiO_2. Appl. Catal., B 2004; 57: 201–9.

[4] Liu N, Yuan Z, Wang S, Zhang C, Wang S, Li D. Characterization and performance of a ZnO–$ZnCr_2O_4$/CeO_2–ZrO_2 monolithic catalyst for methanol auto-thermal reforming process. Int. J. Hydrogen Energy 2008; 33: 1643–51.

[5] Hong X, Ren S. Selective hydrogen production from methanol oxidative steam reforming over Zn-Cr catalysts with or without Cu loading. J. Mol. Catal. A: Chem. 2008; 33: 700–8.

[6] Shishido T, Yamamoto Y, Morioka H, Takehira K. Production of hydrogen from methanol over Cu/ZnO and Cu/ZnO/Al_2O_3 catalysts prepared by homogeneous precipitation: Steam reforming and oxidative steam reforming. J. Mol. Catal. A: Chem. 2007; 268: 185–94.

[7] Patel S, Pant KK. Hydrogen production by oxidative steam reforming of methanol using ceria promoted copper–alumina catalysts. Fuel Process. Technol. 2007; 88: 825–32.

[8] Naknam P, Luengnaruemitchai A, Wongkasemjit S. Preferential CO oxidation over Au/ZnO and Au/ZnO–Fe_2O_3 catalysts prepared by photodeposition. Int. J. Hydrogen Energy 2009; 34: 9838–46.

[9] Yang YF, Sangeetha P, Chen YW. Au/TiO_2 catalysts prepared by photo-deposition method for selective CO oxidation in H_2 stream. Int. J. Hydrogen Energy 2009; 34: 8912–20.

[10] Huang TJ, Chen HM. Hydrogen production via steam reforming of methanol over Cu/(Ce,Gd)O_{2-x} catalysts. Int. J. Hydrogen Energy 2010; 35: 6218–26.

[11] Yi N, Si R, Saltsburg H, Stephanopoulos MF. Steam reforming of methanol over ceria and gold-ceria nanoshapes. Appl. Catal., B 2010; 95: 87–92.

[12] Twigg, MV, Spencer MS. Deactivation of copper metal catalysts for methanol decomposition methanol steam reforming and methanol synthesis. Top. Catal. 2003; 22: 191–203.

[13] Hong X, Ren S. Selective hydrogen production from methanol oxidative steam reforming over Zn-Cr catalysts with or withourt Cu loading. Int. J. Hydrogen Energy 2008; 33: 700–8.

[14] Grisel R, Weststrate KJ, Gluhoi A, Nieuwenhuys BE. Catalysis by gold nanoparticles, Gold Bull. 2002; 35: 39–45.

[15] Lenite BA, Galletti C, Specchia S. Studies on Au catalysts for water gas shift reaction. Int. J. Hydrogen Energy 2011; 36: 7750–8.

[16] Bond GC, Louis C, Thompson DT. Catalysis by Gold, volume 6, Imperial College Press, London, 2006.

[17] Pojanavaraphan C, Luengnaruemitchai A, Gulari E. Hydrogen Production by Oxidative Steam Reforming of methanol over Au/CeO_2 catalysts. Chem. Eng. J. 2012; 192: 105–13.

[18] Srisiriwat N, Therdthianwong S, Therdthianwong A. Oxidative steam reforming of ethanol over Ni/Al_2O_3 catalysts promoted by CeO_2, ZrO_2 and CeO_2–ZrO_2. Int. J. Hydrogen Energy 2009; 34: 2224–34.

[19] Bera P, Hegde MS. Characterization and catalytic properties of combustion synthesized Au/CeO_2. Catal. Lett. 2002; 79: 75–81.

[20] Kongzhai LI, Hua W, Yonggang W, Mingchun L. Preparation and characterization of $Ce_{1-x}Fe_xO_2$ complex oxides and its catalytic activity for methane selective oxidation. J. Rare Earths 2008; 26: 245–9.

[21] Kamimura Y, Sato S, Takahashi R, Sodesawa T, Akashi T. Synthesis of 3-pentanone from 1-propanol over CeO_2–Fe_2O_3 catalysts. Appl. Catal., A 2003; 252: 399–410.

[22] Maluf SS, Nascente PAP, Assaf EM. CuO and CuO–ZnO catalysts supported on CeO_2 and CeO_2–LaO_3 for low temperature water–gas shift reaction. Fuel Proc. Tech. 2010; 91: 1438–45.

[23] Pradhan GK, Parida KM. Fabrication of iron-cerium mixed oxide: and efficient photocatalyst for dye degradation. Int. J. Eng. Sci. Technol. 2010; 2: 53–65.

[24] Neri G, Bonavita A, Rizzo G, Galvagno S, Capone S, Siciliano P. Methanol gas-sensing properties of CeO_2–Fe_2O_3 thin films. Sens. Actuators, B 2006; 114: 687–95.

[25] Tabakova T, Avgouropoulos G, Papavasiliou J, Manzoli M, Boccuzzi F, Tenchev K, Vindigni F, Ioannides T. CO-free hydrogen production over Au/CeO_2–Fe_2O_3 catalysts: Part 1. Impact of the support composition on the performance for the preferential CO oxidation reaction. Appl. Catal., B 2011; 101: 256–65.

[26] Tabakova T, Manzoli M, Paneva D, Boccuzzi F, Idakiev V, Mitov I. CO-free hydrogen production over Au/CeO_2–Fe_2O_3 catalysts: Part 2. Impact of the support composition on the performance in the water-gas shift reaction. Appl. Catal., B 2011; 101: 266–74.

[27] Widmann D, Liu Y, Schüth F, Behm RJ. Support effects in the Au-catalyzed CO oxidation–Correlation between activity, oxygen storage capacity, and support reducibility. J. Catal. 2010; 276: 292–305.

[28] Kunming J, Huili Z, Wencui L. Effect of morphology of the ceria support on the activity of Au/CeO_2 catalysts for CO oxidation. Chin. J. Catal. 2008; 29: 1089–92.

[29] Kim CH, Thompson LT. Deactivation of Au/CeO_x water gas shift catalysts. J. Catal. 2005; 230: 66–74.

[30] Chang FW, Roselin LS, Ou TC. Hydrogen production by partial oxidation of methanol over bimetallic Au-Ru/Fe_2O_3 catalysts. Appl. Catal., A 2008; 334: 147–55.

[31] Jiang XC, Yu AB. Synthesis of Pd/α-Fe_2O_3 nanocomposites for catalytic CO oxidation. J. Mater. Process. Technol. 2009; 209: 4558–62.

[32] Hongyan LIN, Zhiqiang MA, Ling DING, Jieshan QIU, Changhai LIANG. Preparation of nanoscale $Ce_xFe_{1-x}O_2$ solid solution catalyst by the template method and Its catalytic properties for ethanol steam reforming. Chin. J. Catal. 2008; 29: 418–20.

[33] Andreeva D, Tabakova T, Idakiev V, Christov P, Giovanoli R. Au/α-Fe_2O_3 catalyst for water–gas shift reaction prepared by deposition–precipitation. Appl. Catal., A 1998; 169: 9–14.

[34] Haruta M, Kobayashi T, Iijima S, Delannay F. Proceeding 9th Int. Congr. Catal., Calgary, The Chemical Institute of Canada, Ottawa, 1988; 2: 1206.

[35] Fan L, Ichikuni N, Shimazu S, Uematsu T. Preparation of Au/TiO_2 catalysts by suspension spray reaction method and their catalytic property for CO oxidation. Appl. Catal., A 2003; 246: 87–95.

[36] Arena F, Famulari P, Trunfio G, Bonura G, Frusteri F, Spadaro L. Probing the factors affecting structure and activity of the Au/CeO_2 system in total and preferential oxidation of CO. Appl. Catal., B 2006; 66: 81–91.

[37] Biswas P, Kunzru D. Steam reforming of ethanol for production of hydrogen over Ni/CeO_2-ZrO_2 catalyst: Effect of support and metal loading. Int. J. Hydrogen Energy 2007; 32: 969–80.

[38] Xing Z, Hua W, Yonggang W, Kongzhai L, Xianming C. Hydrogen and syngas production from two-step steam reforming of methane over CeO_2-Fe_2O_3 oxygen carrier. J. Rare Earths 2010; 28: 907–13.

[39] Jacobs G, Ricote S, Patterson PM, Graham UM, Dozier A, Khalid S, Rhodus E, Davis BH. Low temperature water-gas shift: Examining the efficiency of Au as a promoter for ceria-based catalysts prepared by CVD of a Au precursor. Appl. Catal., A 2005; 292: 229–43.

[40] Jacobs G, Graham UM, Chenu E, Patterson PM, Dozier A, Davis BH. Low-temperature water–gas shift: impact of Pt promoter loading on the partial reduction of ceria and consequences for catalyst design. J. Catal. 2005; 229: 499–512.

[41] Campo B, Petit C, Volpe MA. Hydrogenation of crotonaldehyde on different Au/CeO_2 catalysts. J. Catal. 2008; 254: 71–8.

[42] Ilieva LI, Andreeva DH, Andreev AA. TPR and TPD investigation of Au/α-Fe_2O_3. Thermochim. Acta 1997; 292: 169–74.

[43] Venugopal A, Scurrell MS. Low temperature reductive pretreatment of Au/Fe_2O_3 catalysts, TPR/TPO studies and behavior in water–gas shift reaction. Appl. Catal., A 2004; 258: 241–9.

[44] Khoudiakov M, Gupta MC, Deevi S. Au/Fe_2O_3 nanocatalysts for CO oxidation: A comparative study of deposition–precipitation and coprecipitation techniques. Appl. Catal., A 2005; 291: 151–61.

[45] Kongzhai L, Hua W, Yonggang W, Dongxia Y. Syngas production from methane and air via a redox process using Ce–Fe mixed oxides as oxygen carriers. Appl. Catal., B 2010; 97: 361–72.

[46] Kongzhai L, Hua W, Yonggang W, Dongxia Y. Transformation of methane into synthesis gas using the redox property of Ce-Fe mixed oxides: Effect of calcination temperature. Int. J. Hydrogen Energy 2011; 36: 3471–82.

[47] Alonso FJP, Cabrera IM, Granados ML, Kapteijn F, Fierro JLG. Synergy of $Fe_xCe_{1-x}O_2$ mixed oxides for N_2O decomposition. J. Catal. 2006; 239: 340–6.

[48] Shan W, Luo M, Ying P, Shen W, Li C. Reduction property and catalytic activity of $Ce_{1-X}Ni_XO_2$ mixed oxide catalysts for CH_4 oxidation. Appl. Catal., A 2003; 246: 1–9.

[49] Fu Q, Kudriavtseva S, Saltsburg H, Stephanopoulos MF. Gold–ceria catalysts for low-temperature water-gas shift reaction. Chem. Eng. J. 2003; 93: 41–53.

[50] Huang XS, Sun H, Wang LC, Liu YM, Fan KN, Cao Y. Morphology effects of nanoscale ceria on the activity of Au/CeO_2 catalysts for low-temperature CO oxidation. Appl. Catal., B 2009; 239: 224–32.

[51] Andreeva D, Idakiev V, Tabakova T, Andreev A. Low-temperature water gas shift reaction over Au/α-Fe_2O_3. J. Catal. 1996; 158: 354–5.

[52] Munteanu G, Ilieva L, Andreeva D. Kinetic parameters obtained from TPR data for α-Fe_2O_3 and Au/α-Fe_2O_3 systems. Thermochim. Acta 1997; 291: 171–77.

[53] Scirè S, Minicò S, Crisafulli C, Galvagno S. Catalytic combustion of volatile organic compounds over group IB metal catalysts on Fe_2O_3. Catal. Commun. 2001; 2: 229–32.

[54] Aneggi E, Leitenburg C, Dolcetti G, Trovarelli A. Promotion effect of rare earths and transition metals in the combustion of diesel soot over CeO_2 and CeO_2–ZrO_2. Catal. Today 2006; 114: 40–7.

[55] Li G, Smith RL, Jr, Inomata H. Synthesis of Nanoscale $Ce_{1-x}Fe_xO_2$ Solid Solutions via a low-temperature approach. J. Am. Chem. Soc. 2001; 123: 11091–2.

[56] Bao H, Chen X, Fang J, Jiang Z, Huang W. Structure-activity relation of Fe_2O_3–CeO_2 composite catalysts in CO oxidation. Catal. Lett. 2008; 125: 160–7.

[57] Zanella R, Giorgio S, Shin CH, Henry CR, Louis C. Characterization and reactivity in CO oxidation of gold nanoparticles supported on TiO_2 prepared by deposition-precipitation with NaOH and urea. J. Catal. 2004; 222: 357–67.

[58] Souza KR, Lima AFF, Sousa FF, Appel LG. Preparing Au/ZnO by precipitation–deposition technique. Appl. Catal., A 2008; 340: 133–139.

[59] Park S, Yoo K, Park HJ, Lee JC, Lee JH. Rapid gold ion recovery from wastewater by photocatalytic ZnO nanopowders. J. Electroceram 2006; 17: 831–34.

[60] Meng M, Tu Y, Ding T, Sun Z, Zhang L. Effect of synthesis pH and Au loading on the CO preferential oxidation performance of Au/MnO_x–CeO_2 catalysts prepared with ultrasonic assistance. Int. J. Hydrogen Energy 2011; 36: 9139–50.

[61] Haruta M, Tsubota S, Kobayashi T, Kageyama H, Genet M, Delmon B. Low-Temperature Oxidation of CO over Gold Supported on TiO_2, α-Fe_2O_3, and Co_3O_4. J. Catal. 1993; 144: 175–92.

[62] Luengnaruemitchai A, Kaengsilalai A. Activity of different zeolite-supported Ni catalysts for methane reforming with carbon dioxide. Chem. Eng. J. 2008; 144: 96–102.

[63] Guisnet M, Magnoux P. Organic chemistry of coke formation. Appl. Catal., A 2001; 212: 83–96.

[64] Faungnawakij K, Kikuchi R, Eguchi K. Thermodynamic evaluation of methanol steam reforming for hydrogen production. J. Power Sources 2006; 161: 87–94.

[65] Armor JN. The multiple roles for catalysis in the production of H_2. Appl. Catal., A 2008; 176: 159–76.